공학박사학위논문

Pattern Recognition-Based Analysis of Free Surface Extensional Flow

패턴인식기반 자유 계면 신장유동 해석

2025년 2월

서울대학교 대학원
화학생물공학부
임 민 혁

공학박사학위논문

Pattern Recognition-Based Analysis of Free Surface Extensional Flow

패턴인식기반 자유 계면 신장유동 해석

2025년 2월

서울대학교 대학원
화학생물공학부
임 민 혁

Pattern Recognition-Based Analysis of Free Surface Extensional Flow

패턴인식기반 자유 계면 신장유동 해석

지도교수 남 재 욱
이 논문을 공학박사 학위논문으로 제출함

2024년 12월

서울대학교 대학원

화학생물공학부

임 민 혁

임민혁의 공학박사 학위 논문을 인준함

2024년 12월

위 원 장	안경현	(인)
부위원장	남재욱	(인)
위 원	이원보	(인)
위 원	김소연	(인)
위 원	김주민	(인)

Abstract

Pattern Recognition-Based Analysis of Free Surface Extensional Flow

Minhyuk Im

School of Chemical and Biological Engineering

The Graduate School

Seoul National University

Understanding and analyzing capillary-driven extensional flow dynamics is essential for applications such as inkjet printing and emulsion formation. However, conventional methods, which often focus on single-point measurements within the slender jet approximation, only partially capture the spatio-temporal evolution of complex fluid shapes during stretching. These shapes, however, contain valuable rheological information. In this study, I introduce novel approaches that integrate machine learning and flow visualization to characterize fluid flows without relying on traditional rheological models. These methods utilize images captured via Dripping Onto Substrate Capillary Break-up Extensional Rheometry (DoS-CaBER), a technique optimized for observing the spatio-temporal dynamics of capillary-driven extensional flows. By analyzing cumulative images and edge curvature, these approaches enable comprehensive extraction of flow information, facilitating an enhanced analysis of the singular dynamics in free-surface extensional flows.

keywords: Extensional flow, Flow visualization, Algorithm, Machine learning
student number: 2021-36497

Contents

List of Tables

List of Figures

Chapter 1

Introduction

In Chapter 1, the capillary-thinning phenomenon of a mixed fluid is captured and transformed into cumulative image data. Principal Component Analysis (PCA) is then applied to extract the Eigenvector that holds the greatest statistical variance across data sets. This approach enables quantification of feature distances of each sample projected within the space aligned with the extracted Eigenvector, thereby facilitating fluid classification and component estimation. Furthermore, this Eigenvector can be utilized for data augmentation, suggesting potential for designing a more robust model. In Chapter 2, the sequence information that cannot be derived from cumulative images is analyzed using a Transformer model, which incorporates an internal attention mechanism. This attention mechanism is utilized to investigate key sequence changes, examining fluid behavior transitions from a contextual perspective. To achieve this, the edge of the fluid curvature, which offers advantages in positional invariance, is extracted and inputted into the model to assess the results.

Chapter 2

Statistical approches from cumulative images

2.1 Introduction

Understanding and analyzing the dynamics of extensional flow driven by capillary forces is essential due to its occurrence in various processes and its significant impact on applications such as inkjet printing, dispensing, and emulsion formation (Dinic *et al.* (2017)). However, the capillary thinning dynamics of fluids exhibit various behaviors in the thinning thread profiles over time, depending on the intrinsic characteristics of the fluid. To model these behaviors, various studies, such as linear stability analysis, similarity solution, and local analysis, have been studied (McKinley (2005); Chang *et al.* (1999); Eggers *et al.* (2020)).

Depending on the properties of fluids under analysis, an appropriate constitutive equation is required. For instance, viscoelastic solutions like dilute poly-ethylene-oxide (PEO) solutions, the Oldroyd-B model is commonly employed to predict their behavior. In the context of local analysis, the Entov-Hinch theory explains the diameter changes of these thinning fluid cylinders (Entov & Hinch (1997)). According to this theory, the variation in the early phase is due to the solvent viscosity and the variation in the middle/late phase follows the elasto-capillary dynamics or the viscous

Newtonian behavior according to the extent of polymer stretching.

Importantly, these fluids are characterized by assuming a uniform slender jet shape. Consequently, the dynamics of these fluids are relatively easy to analyze with their minimum diameter. In this regard, capillary break-up extensional rheometry (CaBER) is widely used for measuring the minimum diameter change over time and this information is utilized to estimate the parameters of extensional rheological models (Rodd *et al.* (2005); McKinley & Sridhar (2002)).

However, complex fluids like shear-thinning fluids with an apparent yield stress exhibit a concave capillary thinning shape influenced by varying Laplace pressures associated with the volume of the extended fluid. This leads to distinct trends in minimum diameter changes along the thread (Niedzwiedz *et al.* (2009)). Therefore, the slender body approximation cannot be applied to these complex fluids.

Meanwhile, the traditional CaBER method analyzes the capillary-thinning dynamics of the liquid bridge formed after stretching the liquid sample loaded between two parallel disks, but it is not applicable to low-viscosity complex fluids with low elasticity($<\sim 20$ mPa $\cdot$ s), where the pinch-off occurs during stretching and the microstructure of the complex fluid is disturbed by the step-strain (Zhang & Calabrese (2022); Dinic *et al.* (2015)). In response to this challenge, the dripping onto substrate capillary break-up extensional rheometry (DoS-CaBER) is proposed, as depicted in Fig. 2.1a. This method involves placing a drop of low-viscosity fluid on a substrate to induce extensional flow with minimal disturbance on its microstructure (Dinic & Sharma (2020)).

However, a typical analysis using DoS-CaBER is also based on the minimum diameter change over time, and the interpretation of the fluid behavior by estimating parameter with the proposed rheological model is not different from that of the CaBER analysis. Consequently, it is difficult, or at least slow, to characterize the dynamic behavior of the entire fluid filament, especially in the case of fluid mixtures such as

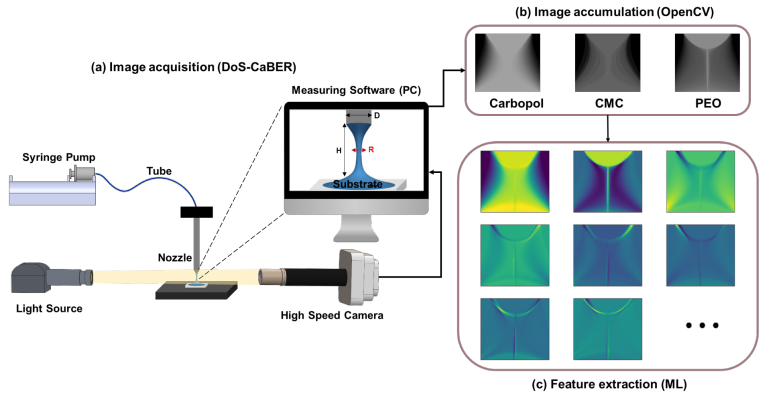

(a)

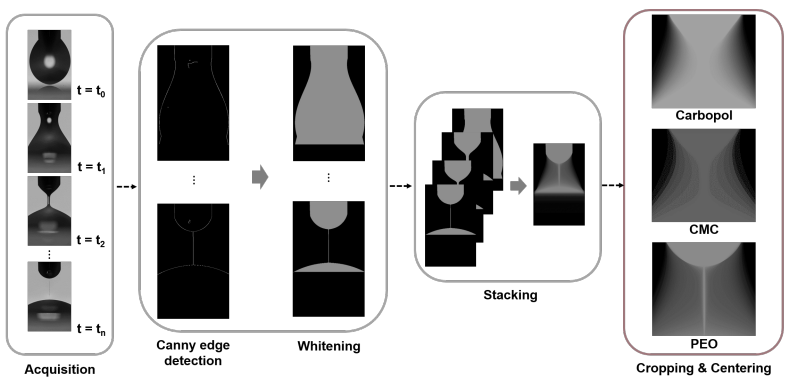

(b)

Figure 2.1: Schematic representation of the pattern recognition process of capillary-driven extensional flow and image stacking process. (a) Image acquisition was performed through dripping onto substrate capillary break-up extensional rheometry (DoS-CaBER). Acquired images were stacked using custom Python code (OpenCV).

particle suspensions and polymer solutions. A notable exception is the analysis of the *beads-on-a-string* (BOAS) phenomenon, which is performed by computational analysis rather than experimental methods(Bhat *et al.* (2010)).

In this study, we present a new technique that focuses on using capillary-driven extensional flow visualization to observe the holistic dynamics of complex fluids, and leveraging ML to extract rheological information from the accumulated images, as depicted in Fig. 2.1a. By stacking all the frames taken by a high-speed camera, through the processes shown in Fig. 2.1b, the temporal evolution of the flow shape can be encapsulated in a single image. Notably, fluids with distinct properties exhibit unique stacked images. Considering the complex interplay of surface tension force, viscous force, and visco-elastic force affecting the fluid's edge on liquid-air interfaces, these stacked images could serve as a promising fountainhead for fluid classification and estimation.

Inspired by the eigenface technique, which extracts facial features for human face recognition (Zhang *et al.* (1997); Singh & Kumar (2012)), we introduce the concept of *eigenthinning*. In this study, we use principal component analysis (PCA) to extract these modes and apply for classification and composition estimation using the k-nearest neighbor (kNN) classifier method (Abdi & Williams (2010); Dino & Abdulrazzaq (2019)). Furthermore, we could generate artificial images through modes and enhance the accuracy of the model using this reinforced dataset.

Some studies have been conducted to analyze and predict the complex and transient dynamics of droplets in the air stream, visualizing them by in-line digital holography and characterizing them by analytical model and ML-based method (Ade *et al.* (2024, 2023); Gao *et al.* (2013); Guildenbecher *et al.* (2017)).

Similarly, this study provides a new perspective for analyzing the behavior of fluids that are difficult to analyze solely on the basis of minimum radius due to their irregularity at the pinch-off region. It could also be used for quality control in in-

dustrial settings where rapid analysis is required, as it can identify the approximate composition or state of unknown fluids based on trained data without reference to a rheological model.

2.2 Materials and Methods

Sample preparation

Table 2.1: Class-wise weight ratio of the multicomponent fluids. The total weight is set to 1 representing the weight ratios of each solution. The conctration of aqueous Carbopol (Lubrizol Korea, Inc.) solution is 0.14 %. The concentration of aqueous sodium carboxymethyl cellulose ($M_w \sim 2.5 \times 10^5$ g/mol, Sigma Aldrich, Germany) solution is 1 %. The concentration of aqueous poly ethylene oxide ($M_v \sim 2.0 \times 10^6$ g/mol, Sigma Aldrich, Germany) solution is 1 %.

Solution	Class 1	Class 2	Class 3	Class 4	Class 5	Class 6	Class 7
Carbopol	1	0	0	1/2	1/2	0	1/3
CMC	0	1	0	1/2	0	1/2	1/3
PEO	0	0	1	0	1/2	1/2	1/3

DoS-CaBER measurment.

Extensional flows and pinch-off dynamics were observed using the dripping onto substrate capillary break-up extensional rheometry(DoS-CaBER) system, as depicted in Fig. 2.1a. For monitoring fluid capillary thinning and pinch-off dynamics, an optical system was employed. This system consisted of a high-speed camera (VEO 710L, Phantom, USA), a long-distance microscope lens (5×; 59876, Edmund Optics, USA), and an illuminator (125W, LED light source, NeXber, Korea). In the flow

system, a 5 ml syringe (NORM-JECT, Henke Sass Wolf, Germany) acted as a fluid reservoir, and a syringe pump (Harvard Apparatus, USA) controlled the fluid flow rate. A stainless-steel nozzle (18 gauge; ID: 0.000833 m, OD: 0.00127 m, Hamilton, USA) was used to deliver the fluid to a substrate (76×26×1 mm, Microscope slides, Marienfeld, Germany). The syringe was connected to the stainless-steel nozzle via a Tygon tube (ID: 0.00127 m, OD: 0.00228 m, TYGON^{TM}). The distance between the nozzle end and the top of the substrate was set to three times the nozzle OD. The fluid was delivered at a flow rate of 0.2 ml/hour, and the pumping was halted as soon as the fluid contacted the substrate. Subsequently, a liquid bridge formed between the nozzle and the substrate, undergoing capillary thinning and pinch-off. These phenomena were recorded using the high-speed camera at a speed of 10,000 fps, with an exposure time of 1 μs. The recorded images were processed using OpenCVOpenCV Development Team (2021) and custom Python code(https://github.com/ttackpoo/capillary_thinning).

Image preprocessing.

The images obtained from the DoS-CaBER system underwent several processing steps. First, the outline of the capillary thinning image was extracted using Canny edge detection (Canny (1986)) implemented in OpenCV (OpenCV Development Team (2021)). Then, the interior of this outline was whitened to eliminate any noise stemming from the lighting and shooting conditions.

To store information proportional to the number of stacking images, the accumulated pixel intensity values were rescaled by dividing them by the scaling parameter. The scaling parameter was set to 8,000, which corresponds to the number of frames captured during the longest process time observed in the Carbopol solution, preventing any loss of information due to the accumulated intensity values exceeding the upper limit of 255.

Because PCA depends on the pixel coordinate in which the data is represented, image alignment and cropping are necessary for consistent results. To do this, the minimum and maximum values of the x-coordinates of the images are collected according to the y-coordinates and then averaged to calculate the center line. Based on this measurement, the image was cropped and aligned around this center line.

PCA, kNN and data augmentation.

Principal component analysis (PCA) and k-nearest neighbour (kNN) methods were implemented using the scikit-learn library (Pedregosa *et al.* (2011)). The process involved vectorizing each accumulated sample image to create an n-by-m matrix, where n represents the number of pixels and m represents the number of samples.

Mean subtracted image matrix $\mathbf{B}$ is determined as

$$\mathbf{B} = \mathbf{X} - \bar{\mathbf{X}} = \begin{bmatrix} x_{11} - \mu & x_{12} - \mu & \cdots & x_{1m} - \mu \\ x_{21} - \mu & x_{22} - \mu & \cdots & x_{2m} - \mu \\ \vdots & \vdots & \ddots & \vdots \\ x_{n1} - \mu & x_{n2} - \mu & \cdots & x_{nm} - \mu \end{bmatrix} \tag{2.1}$$

where $\mathbf{X}$ and $\bar{\mathbf{X}}$ represent the matrices of the images and the mean matrix, respectively, while x and μ denote the pixel intensities of the images and their mean, respectively.

The matrix $\mathbf{B}$ can be decomposed using singular value decomposition (SVD) into

$$\mathbf{B} = \mathbf{U}\mathbf{\Sigma}\mathbf{V}^{\mathrm{T}} = \begin{bmatrix} \mathbf{u}_1 & \mathbf{u}_2 & \cdots & \mathbf{u}_n \end{bmatrix} \begin{bmatrix} \sigma_1 & 0 & \cdots & 0 \\ 0 & \sigma_2 & \cdots & 0 \\ \vdots & \vdots & \ddots & \vdots \\ 0 & 0 & \cdots & 0 \end{bmatrix} \begin{bmatrix} \mathbf{v}_1^{\mathrm{T}} \\ \mathbf{v}_2^{\mathrm{T}} \\ \vdots \\ \mathbf{v}_m^{\mathrm{T}} \end{bmatrix}. \tag{2.2}$$

where the columns of $\mathbf{U}$ are called *left singular vectors* of $\mathbf{B}$ and the columns of $\mathbf{V}$ are *right singular vectors*. The diagonal elements of $\mathbf{\Sigma}$ are *singular values* and they are ordered from largest to smallest.

The rank of $\mathbf{B}$ is equal to the number of nonzero singular values. After selecting an appropriate value of r, which represents the desired number of singular vectors, truncated SVD can be performed, resulting in an approximated matrix $\widetilde{\mathbf{B}}$:

$$\widetilde{\mathbf{B}} = \widetilde{\mathbf{U}}\widetilde{\mathbf{\Sigma}}\widetilde{\mathbf{V}}^{\mathrm{T}} = \begin{bmatrix} \mathbf{u}_1 & \mathbf{u}_2 & \cdots & \mathbf{u}_r. \end{bmatrix} \begin{bmatrix} \sigma_1 & 0 & \cdots & 0 \\ 0 & \sigma_2 & \cdots & 0 \\ \vdots & \vdots & \ddots & \vdots \\ 0 & 0 & \cdots & \sigma_r \end{bmatrix} \begin{bmatrix} \mathbf{v}_1^{\mathrm{T}} \\ \mathbf{v}_2^{\mathrm{T}} \\ \vdots \\ \mathbf{v}_r^{\mathrm{T}} \end{bmatrix}. \tag{2.3}$$

PCA is conducted by determining the covariance matrix $\widetilde{\mathbf{C}}$ as

$$\widetilde{\mathbf{C}} = \widetilde{\mathbf{B}}\widetilde{\mathbf{B}}^{\mathrm{T}} = \widetilde{\mathbf{U}}\widetilde{\mathbf{\Sigma}}^2\widetilde{\mathbf{U}}^{\mathrm{T}} \tag{2.4}$$

where $\widetilde{\mathbf{C}}$ is

$$\widetilde{\mathbf{C}} = \begin{bmatrix} \mathbf{u}_1 & \mathbf{u}_2 & \cdots & \mathbf{u}_r \end{bmatrix} \begin{bmatrix} \sigma_1^2 & 0 & \cdots & 0 \\ 0 & \sigma_2^2 & \cdots & 0 \\ \vdots & \vdots & \ddots & \vdots \\ 0 & 0 & \cdots & \sigma_r^2 \end{bmatrix} \begin{bmatrix} \mathbf{u}_1^{\mathrm{T}} \\ \mathbf{u}_2^{\mathrm{T}} \\ \vdots \\ \mathbf{u}_r^{\mathrm{T}} \end{bmatrix}. \tag{2.5}$$

where eigenvectors $\mathbf{u}_i (i = 1, ..., r)$ are the *principal components*. The first principal component $\mathbf{u}_1$ is the eigenvector of the covariance matrix corresponding to the largest squared singular value σ_1^2.

The score matrix $\mathbf{Z}$, determined as

$$\mathbf{Z} = \mathbf{B}^T\widetilde{\mathbf{U}} = \begin{bmatrix} x_{11} - \mu & x_{21} - \mu & \cdots & x_{n1} - \mu \\ x_{12} - \mu & x_{22} - \mu & \cdots & x_{n2} - \mu \\ \vdots & \vdots & \ddots & \vdots \\ x_{1m} - \mu & x_{2m} - \mu & \cdots & x_{nm} - \mu \end{bmatrix} \begin{bmatrix} \mathbf{u}_1 & \cdots & \mathbf{u}_r \end{bmatrix} = \begin{bmatrix} Z_{11} & \cdots & Z_{1r} \\ \vdots & \cdots & \vdots \\ Z_{m1} & \cdots & Z_{mr} \end{bmatrix}. \tag{2.6}$$

where Z represents the scores of each sample in the r-dimensional space of the principal components.

The approximately regenerated dataset matrix $\widetilde{\mathbf{X}}$ can be determined as

$$\widetilde{\mathbf{X}} = \mathbf{Z}\widetilde{\mathbf{U}}^T + \bar{\mathbf{X}} \tag{2.7}$$

and the artificial dataset matrix $\mathbf{X}_{\text{new}}$ can be determined as

$$\widetilde{\mathbf{X}}_{\text{new}} = \mathbf{Z}_{\text{rand}}\widetilde{\mathbf{U}}^T + \bar{\mathbf{X}}. \tag{2.8}$$

In this study, $\mathbf{Z}_{\text{rand}}$ is the normally distributed randomized score matrix, where the appropriate scores Z are chosen with reference to their means and half of their standard deviations.

In kNN, the class of a test sample is predicted based on the number of nearest neighbors from the training set in the space of principal components. The threshold value for this determination is denoted as k. The classification model makes its final decision through a majority vote rule. In the estimation model, the probability of belonging to a specific class is determined by considering the ratio of nearest neighbor samples selected from the total k value. The Euclidean distance serves as the criterion for identifying the nearest neighbors to the test sample, determined as

$$d(\mathbf{z}_r^p, \mathbf{z}_r^q) = \sqrt{(Z_1^q - Z_1^p)^2 + (Z_2^q - Z_2^p)^2 + \cdots + (Z_r^q - Z_r^p)^2}. \tag{2.9}$$

where $\mathbf{z}_r^p$ and $\mathbf{z}_r^q$ represents row vectors of the score matrix $\mathbf{Z}$ of the image $\mathbf{p}$ and $\mathbf{q}$, respectively. This calculation involves summing the squares of the differences between the coordinate values in each dimension in which the sample is projected and then taking the square root.

Rheological properties.

The loss modulus $\mathbf{G}''$ was measured using a stress-controlled rheometer (Discovery HR-2, TA Instruments Inc.) equipped with parallel 40-mm plates and a gap of approximately 1 mm. To prevent water evaporation from the samples, an acrylic cover was employed. The amplitude sweep test was performed with strain oscillations of $\sim$ 10 % at a frequency of 6.27 rad/s, a range in which the target fluids exhibit only linear viscoelasticity. The results are briefly attached in Fig. S7. The extensional viscosity η can be determined as

$$\eta_{\text{E}} = \frac{\sigma}{\dot{\varepsilon}R} = \frac{\sigma}{-2dR(t)/dt}. \tag{2.10}$$

where σ, $\dot{\varepsilon}$ and R are the surface tension, hencky strain rate, and minimum radius of the thread, respectively. The extension rate $\dot{\varepsilon} = -2d\ln R(t)/dt$ is obtained from the radius evolution plots. The point at which the extensional viscosity-Hencky strain plot exhibits a constant region was selected as the representative extensional viscosity.

2.3 Results

Eigenthinning Analysis

For clarity of characterization, each unique and distinct fluid was chosen as a demonstration sample: polyethylene oxide (PEO) solution for viscoelastic fluids, carboxymethylcellulose (CMC) for shear-thinning fluids, and Carbopol 941 solution for shear-thinning with yield stress fluids (McKinley (2005)). Each single-component fluid with different properties is mixed in predetermined weight ratios and categorized into seven classes as shown in Tab. 2.1. For each class, a total of 30 videos are recorded and processed to create cumulative images according to the procedure shown in Fig. 2.1b. Then, each image is vectorized and subjected to mean subtraction and matrixsified, as illustrated in (2.1). Through principal component analysis (PCA) based on singular value decomposition (SVD), the principal components(PC), which represents *eigenthinning* mode, are extracted and visualized as shown in the Fig. 2.2a.

The first principal component (PC1) represents the direction of the largest variance in the image dataset. The second principal component (PC2) is orthogonal to PC1 and represents the direction of the next largest variance. This pattern continues for subsequent PCs and each principal component explains the variance that is not captured by the other principal components.

High-rated PCs, such as PC1 and PC2, effectively capture significant features like concave shapes and uniform thread shapes. On the contrary, low-rated principal components, particularly those beyond PC3, highlight more intricate details, such as the boundaries of the main droplet and the profiles of threads. Local heterogeneities of complex fluids make their filaments more sensitive to perturbations than others, leading to irregularities in these features. These nuances have typically been studied in the context of linear stability analysis (Muddu *et al.* (2012)).

By projecting each stacked image onto PCs, as shown in (2.6), the samples with similar shape to PCs are assigned to get the higher score value or coordinate value, otherwise to get the lower score value, so that the image data is placed in the space characterized by PCs. This allows us to use the kNN algorithm with a a Euclidean distance defined by (2.9).

To determine the interpretability for PCs, a relative comparison with rheological proper-

ties was examined. The average score value for each PC was compared with the loss modulus in linear viscoelastic region and extensional viscosity. As depicted in Fig. 2.2b, the average score values for PC1 across different classes exhibit a similarity to the variation in the loss modulus. The shape of the PC1 image, shown on the left, exhibits a similarity to the early stages of capillary thinning of viscoelastic fluid, described in Entov-Hinch theory, which are influenced by the shear viscosity of the fluid (Entov & Hinch (1997)).

As described in the Materials and Methods section, the comparative loss modulus was measured in the linear viscoelasticity region at a frequency of 6.27 rad/s, with a strain oscillation of $\sim$ 10 % in the amplitude sweep. The loss modulus in this region can be related to the shear viscosity, indicating that through PC1, a relative comparison of the loss modulus between the measured fluids can be made, even though it does not provide absolute values.

Likewise, PC2 can be regarded as containing information that determines the distinction in extension viscosity among samples.

The results presented above demonstrate that the feature information extracted from the several eigenthinning modes can be effectively correlated with rheological property information.

Classification Problem

The primary objective of the classification problem is to achieve precise differentiation among the seven distinct classes detailed in Tab. 2.1, utilizing the k-Nearest Neighbors (kNN) algorithm illustrated in Fig. 2.3a. This problem can be solved by projecting the data set onto an eigenthinning extracted by Principal Component Analysis (PCA) from a seven-class training set, and then comparing the distance between the train and the test data using the kNN algorithm. This algorithm assumes that the closer the Euclidean distance between the projected data points in the eigenspace, the more similar the samples are to each other.

Model accuracy was computed as the ratio of correct predictions, determined by the majority vote rule of the kNN algorithm, to the total number of test samples. The ratio of test samples to training samples was set at 10 %.

The accuracy graphs, depicted in Fig. 2.4a, showcase the impact of the number of principal components (PCs) and the hyperparameter k on classification accuracy. Notably, the

results indicate that fluid classification attains nearly 100 % accuracy using fewer than 10 PCs and an appropriate value of k. However, as the number of PCs and k increase beyond this optimal point, accuracy gradually diminishes. This observed trend is attributed to the potential for overfitting or underfitting as the values of PCs and k change.

An increase in the number of PCs leads to an expansion of the eigenspace, resulting in larger distances between data points. Consequently, the model becomes more sensitive to variations within training sets, potentially leading to overfitting. Conversely, an elevated value of k, as shown in Fig. 2.4b, results in the opinions of other next nearest neighbors overshadowing those of the nearest neighbors. This scenario, indicative of underfitting, leads to suboptimal results. In our specific case, the graph highlights that approximately 10 key PCs effectively capture the primary features essential for accurate classification. Optimal values for the number of PCs and the k parameter can be determined through other robust methods such as bootstrapping or cross-validation (James *et al.* (2013)).

In sum, this analysis underscores the straightforward yet effective nature of the classification model, setting the stage for subsequent discussions in the study. Interestingly, the subsequent estimation model discussed in the following section requires a higher number of PCs compared to the classification model. This observation emphasizes the need for a more comprehensive set of features to handle more intricate problems.

Component Estimation Problem

The component estimation problem involves accurately estimating the proportions of components in a multicomponent test sample that includes untrained samples. Unlike the classification problem, this problem can be solved using eigenthinning modes extracted from only three classes of single-component liquids listed in Tab. 2.1. The k-nearest neighbors (kNN) algorithm calculates the probabilities, which are considered to be the mixing ratios of the test samples, of belonging to each single-component class for all seven-class test samples.

The output of the model consists of a tuple with three elements expressed by the probability of belonging to these classes. The design described above enables each element of the tuple to represent the model's estimation. Compared to the error-filtering effect driven by the majority vote principle within the classification model, it interestingly offers the advantage

of conducting a more detailed examination of the impact of bias and hyperparameter settings on model accuracy improvement.

We set the hyperparameter k to 6 to represent the denominators of the component ratios for each sample. Here, 6 is the least common multiple of the possible denominators in the output. The fractions we aim to predict with this model include 0, 1, 1/2, and 1/3, as indicated in Tab. 2.1. For example, if the test sample belongs to class 7 with the label (1/3, 1/3, 1/3), and the model correctly estimates it, the output will be (2/6, 2/6, 2/6), as illustrated in Fig. 2.3b. Like the classification model, the ratio of test samples to training samples was set at 10 $\%$.

The results of estimating the composition of test samples are shown in Fig. 2.5a. As depicted in Fig. 2.5a(PC15-0F-0W), the model successfully estimates the trained single-component fluid classes. However, it exhibits some errors for untrained classes, which are multi-component fluids. For instance, the model erroneously predicts class 4 as class 2, which is single-component fluid CMC. Apparently, the model failed to capture the distinguishing feature between class 2 and class 4, which is the *beads-on-a-string* (BOAS) caused by perturbation before the breakup (McKinley (2005)).

This limitation is attributed to our model's reliance on the pixel intensity of the stacked image, where cumulative values of intensities for temporal characteristics like BOAS, occurring in a brief moment of about a microsecond, can be overshadowed by other snapshot frames. Such features need to be highlighted in order for principal components (PCs) to capture them effectively. Specifically, we emphasize several frames that possibly contains BOAS features. In this study, the pixel intensity of the last 10, 30, and 50 frames before the pinch-off are multiplied by the prescribed weight. The weight value is set to 100 because it yields the smallest mean square error (MSE) of the estimates comparing to other weight values, according to the numerical experiment summarized in Fig. S11-S12 in the Supporting Information.

The estimation setup is labeled 'PC-F-W', which is explained in Fig. 2.5, and we will use this notation throughout. As shown in Fig. 2.5a(PC15-10F-100W), there is some improvement in the estimation accuracy for class 4, but the accuracy for the remaining multi-component fluids remains low. To address this issue, we choose the number of PCs different from the original unweighted model because the emphasized featured need additional PCs to be captured properly.

As a result, the added PCs slightly decreased the accuracy for some single component fluids, but increased the accuracy for multi-component fluids, as shown in the PC25-10F-100W, PC25-30F-100W and PC35-10F-100W setup.

The reduced accuracy in single-component fluids results from overfitting, stemming from the inclusion of minor principal components (PCs) that contain detailed information, as previously explained in the classification model. However, these components remain essential for accurate estimation of multi-component fluids.

The method described earlier is basically a bias setting based on user observations with a prior knowledge for enhancing the distinguishment of Class 2 and Class 4 classes. In general, it is better to find the optimal frame and pixel intensity that captures important features adaptively. This adaptive weighting can be achieved by applying a recurrent neural network (RNN) model that takes each frame as input (Medsker & Jain (2001)).

Since the above result is an example of one of the pseudo-randomized training-test sample splits, we plotted a boxplot of the mean square error over 30 random splits as part of a k-fold cross-validation to increase confidence in our model performance evaluation, and the results are shown in Fig. 2.5b. The number of PCs is increased by 10 from 5 to 55, and the visualized 5^{th}, 15^{th}, 25^{th}, 35^{th} PCs are described in Fig. S13 - S15 in Supporting Information.

The box plots plotted on each PCs are color-coded according to the number of weighted frames. The results indicate that the lowest median values were observed when we applied weights equivalent to 100, which is multiplied to the pixel intensity to the last 10 frames before the break and used 35 PCs for estimation.

Among the weighted frame setups, the 50-frame setup tends to have an increased MSE compared to the 10-frame and 30-frame setups. For this setup, the increased error can be attributed to pixel values saturating in the vicinity of important frames when additional weighted frames are introduced, as depicted in Fig. S16. This saturation blurs the interfacial shape, which in turn has a negative impact on the accuracy of concentration estimation.

The approach presented in this section is simple yet effective for concentration estimation, allowing for intuitive parameter optimization. Furthermore, additional methods can be explored to further minimize the persistent error, such as implementing adaptive weights per frame. This will improve the accuracy of the model, allowing it to better capture subtle differences between classes.

Data augmentation

In addition to the findings mentioned earlier, principal components (PCs) can be a valuable tool for creating augmented training datasets. As shown in Fig. 2.5a(PC25-30F-100W(aug)) and Fig. 2.5b(bottom), we see some improvement when we estimate the concentration after augmenting the training sets by 130 %.

Box plots of mean squared error (MSE) show decreased trend compared to normal data set. Among them, PC25-30F-100W setup shows the lowest mean value of MSE. Possibly, the PCs extracted from the augmented training set can provide more diversity to the estimation model, so that fewer PCs are needed for the best estimation.

The process of data augmentation involves making the score matrix (denoted as the matrix Z), as indicated by (2.6). Each column of the matrix corresponds to the scores of samples for each principal components. By randomizing the scores with a normal distribution referenced by mean and standard deviation of them, artificial sample images can be generated as shown in (2.8). The effectiveness of this approach is illustrated in Fig. 2.5c, where the augmented samples demonstrate enhanced detail as more principal components (PCs) are employed in the reconstruction.

This data augmentation method holds particular relevance for learning models that demand substantial amounts of data, such as neural networks. Furthermore, the efficiency of the reconstruction method underscores the capacity of principal components (PCs) to efficiently store image data, even when dealing with datasets that consume significant memory.

2.4 Discussion

The main difference in the eigenthinning mode between the two models lies in whether the multi-component fluids are included in the training set. Multi-component fluids exhibit more pronounced characteristics during capillary thinning. As thinning flow progresses, the space available for fluid flow narrows, making even well-mixed mixtures highly sensitive to minor experimental perturbations, as localized heterogeneities emerge within this confined geometry.

Such characteristic of mixture may complicate the phenomena like BOAS by introduc-

ing beads in irregular positions and showing motions quite different even within the same classes, as depicted in Fig. 2.6. This complexity can negatively impact classification accuracy as the model learns, especially when lower-ranked principal components are employed for classification, potentially leading to overfitting. The difficulty in quantifying these minor PCs with conventional rheological properties is also attributed to this complexity.

Although not directly related to rheological properties, high-ranked PCs in the classification model, especially those higher than ten, are thought to contribute to classification by capturing distinctive shapes caused by perturbations. These distinctive shapes appear to arise from the rheological properties of complex fluids. These nuances can be difficult to classify using traditional methods. Meanwhile, PCs below about the top ten are expected to capture not only small details of the thinning flow, but also variations due to experimental noise as discussed above, potentially leading to model overfitting. In this way, significant PCs that are challenging to define using conventional rheological properties can be cherry-picked and utilized for fluid classification.

On the other hand, the concentration estimation model was trained using single-component fluids, which are relatively stable in comparison. Therefore, extracted eigenthinning modes, despite lower ranks, can not only better differentiate the variations induced by complex fluid samples but also enhance the accuracy of the model with weighted important frames. According to our results, these PCs from pure samples are enough for estimating the fluid's composition, even when dealing with untrained samples.

While we may not provide comprehensive rheological explanations for the lower rank PCs in both problems, it is important to recognize that these eigenthinning modes capture subtle differences primarily induced by perturbations from material inhomogeneity or experimental noise. These nuances, although challenging for human observation, may contain essential information about the behavior of complex fluids. This insight underscores the importance of our study's approach, which leverages these subtle differences to do certain interesting applications such as fluid classification and predicting composition, beyond what is achievable with standard rheological methods.

Additionally, the PCs can be utilized for data augmentation, strengthening the estimation model. This implies that PCs inherently contain information from the actual data.

Furthermore, the models used in this study successfully achieved accurate results despite

the variables introduced by the fluid mixture, such as the stability of the Carbopol hydrogel system, which can be crucially affected by the salt present in CMC solutions(Kolarova Raskova *et al.* (2016)). In other words, despite our model relying on linear predictions, it successfully produced reasonable results for a complex phenomenon wherein the viscosity of complex fluids actually decreases as single-component fluids mix.

Compared to advanced image classification models utilizing convolutional neural networks (CNNs) (O'shea, Keiron and Nash, Ryan (2015)), whose feature analysis is relatively challenging, this study emphasizes intuitiveness and explainability. It aligns with the current trend of creating interpretable models, serving as an initial step towards crafting explainable deep learning models like explainable visual attention networks (VANs) (Guo *et al.* (2022)) for image captioning or explainable recurrent neural networks (RNNs) for video analysis (Medsker & Jain (2001)).

The pattern recognition machine learning model proposed in this study could find applications in inspecting inkjet printing and contactless dispensing processes, where fluid properties change over time, and quick repeatability is crucial. These approaches also have the potential to enhance the estimation of rheological properties in complex fluids, offering more comprehensive insights compared to conventional methods that rely on minimal diameter measurements. Overall, these findings open avenues for the rapid characterization of fluid properties and the automated adjustment of optimal process conditions.

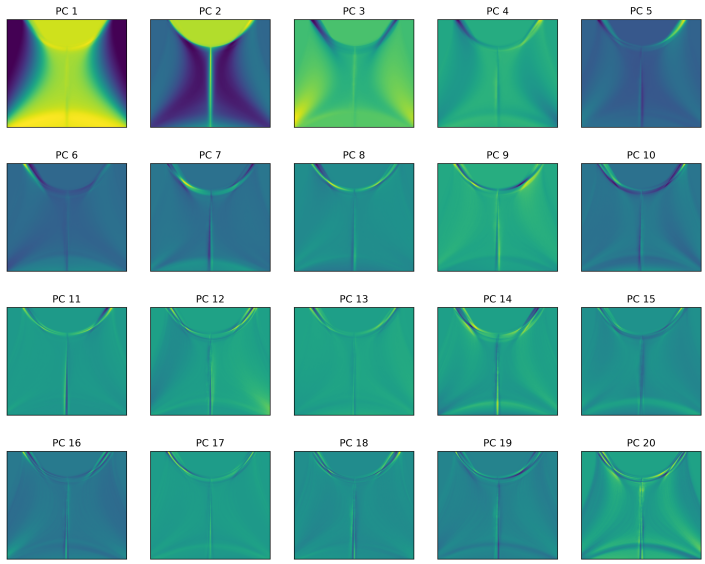

(a) Top twenty principal components(eigenthinning) of the processed capillary thinning images.

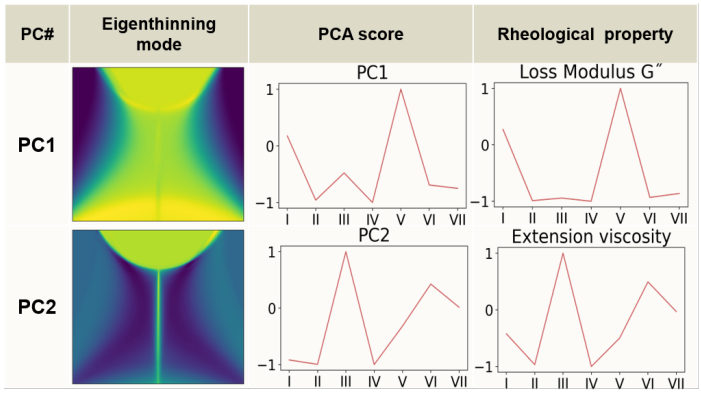

(b) Comparison between PCA score and rheological properties.

Figure 2.2: Eigenthinning Analysis. (a)The components are orthogonal to each other in the eigenspace and each component explains the variance that is not captured by the other components.(b) The left column represents visualized eigenthinning mode, the middle column shows PCA scores (calculated based on (2.6)), and the right column displays rheological properties.

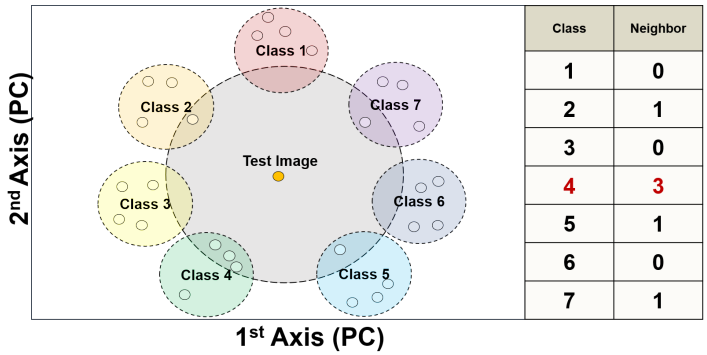

Class	Neighbor
1	0
2	1
3	0
4	3
5	1
6	0
7	1

(a) Classification problem.

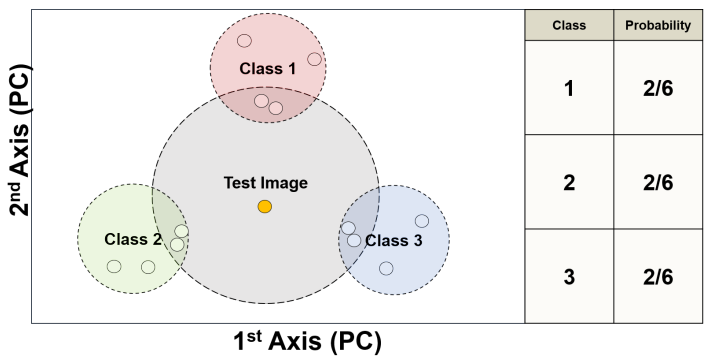

Class	Probability
1	2/6
2	2/6
3	2/6

(b) Estimation problem.

Figure 2.3: Graphical illustration of an example classification and estimation model using the k-nearest neighbor method with two axes and classification results. Note that each circle represents a data point projected using eigenthinning modes, and for simplicity, the number of modes (PC axes) being projected is limited to two. (a) The classification model, the gray circles represent the radius centered on the test image score, and within this radius, the projected scores for each class are depicted. The table on the right displays the outcomes of the majority vote, determined with k set to 6. Consequently, Class 4, which received the highest number of votes, is the classification result. (b) The estimation model, it expresses the results by calculating the ratio of the nearest neighbors of each class to the hyperparameter k, which represents the probability of the test sample belonging to each class in the right table.

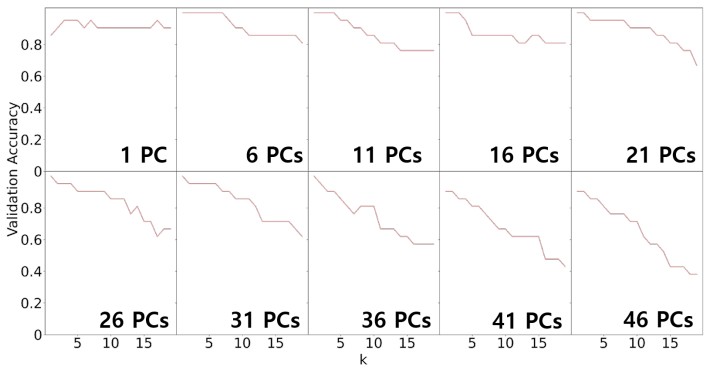

(a)

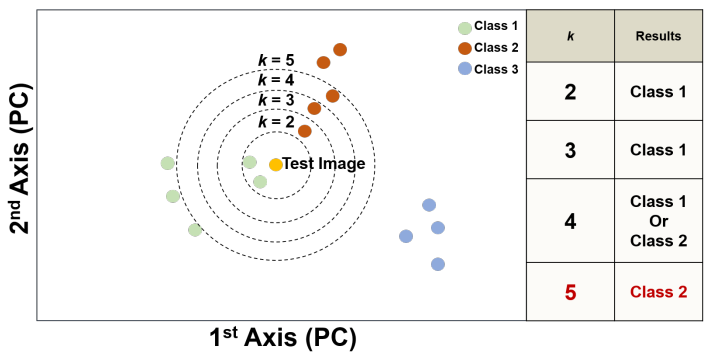

(b)

Figure 2.4: (a) Classification accuracy with respect to the number of eigenthinning modes(PC) and neighborhoods(k). 'PC' stands for the number of the PCs used starting from the first in incremental order. (b) The kNN classifier results according to k parameter. When the k increases, the classification results changed from Class 1 to Class 2 as shown on the right table.

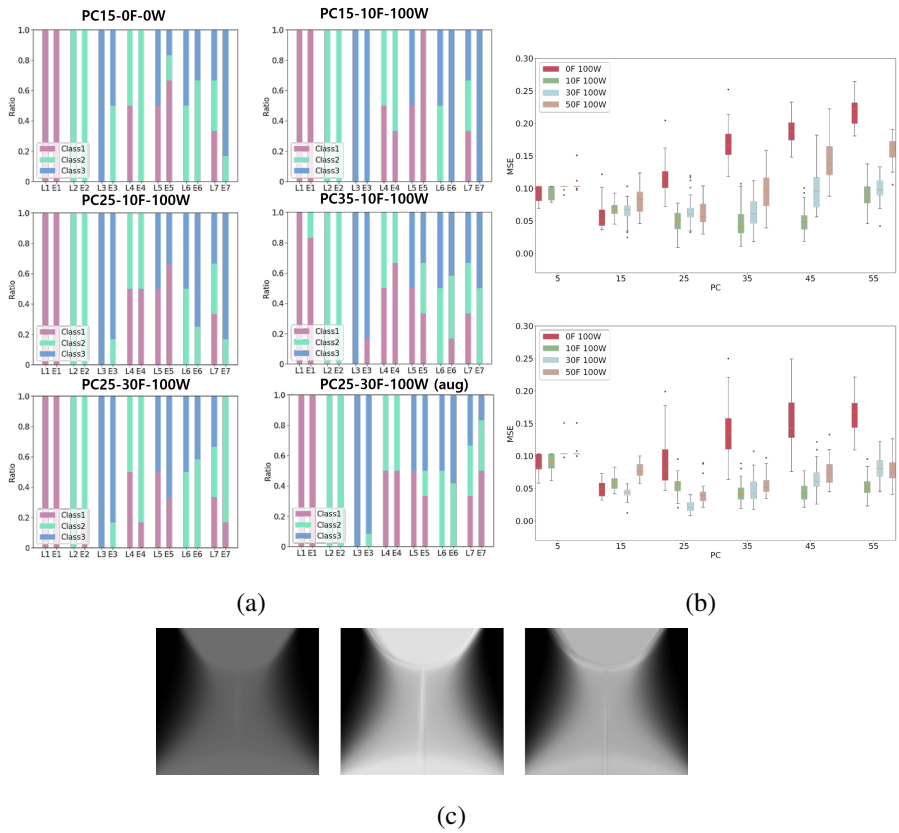

Figure 2.5: (a) Concentration estimation results for different weighting strategies. The labels include 'PC' for the number of principal components, 'F' for emphasized frames, 'W' for the weight factor applied to these frames, 'L' as the dataset label, 'E' for estimation results, and '(aug)' for results from the augmented dataset. (b) Box plots depict the mean squared error of the estimation model based on the number of principal components used. The top panel displays results labeled as 0F-100W (in red), 10F-100W (in green), 30F-100W (in light blue), and 50F-100W (in pink). The bottom panel shows corresponding box plots with a 30 percent train set augmentation. (c) Artificial image samples were generated using the first three modes (3 PCs), 30 modes, and 60 modes, progressing from left to right.

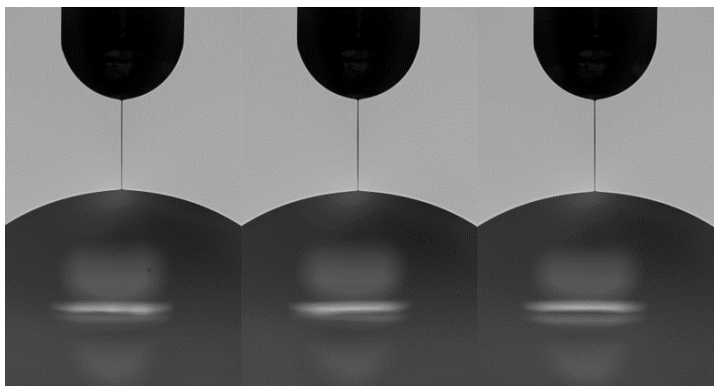

(a)

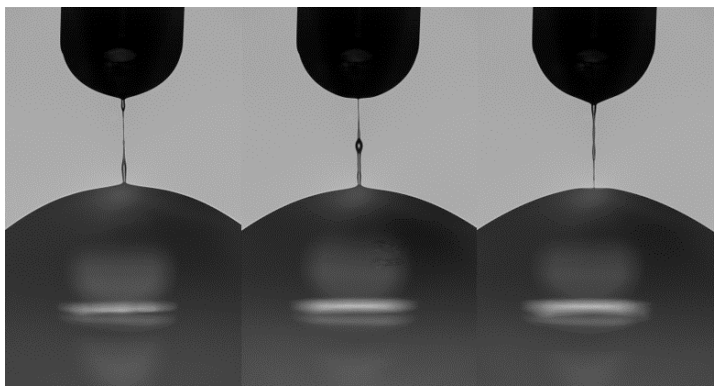

(b)

Figure 2.6: Last frames before the pinch-off captured by DoS-CaBER. (a) The last frames captured by DoS-CaBER before the pinch-off of the CMC solution (Class 2) samples exhibit a long straight thread shape. (b) In contrast, the Carbopol and CMC mixture solution (Class 4) shows the irregular thread structure.

Chapter 3

Contextual approach with time series evolving curvature

3.1 Introduction

The approach of extracting information from accumulated images lacks robustness in terms of position invariance and misses information about critical moments. To address these limitations, we extract information based on curvature.

The curvature of a fluid undergoing extensional flow can be defined as follows.

$$\kappa_{\text{axial}} = \frac{1}{R_{\text{axial}}} = -\frac{h_{zz}}{(1+h_z^2)^{3/2}} \tag{3.1}$$

$$\kappa_{\text{azimuthal}} = \frac{1}{R_{\text{azimuthal}}} = \frac{1}{h\sqrt{1+h_z^2}} \tag{3.2}$$

where h_{zz} and h_z are the second and first derivatives of the radius with respect to the z-direction, respectively.

The p can be defined as

$$p = \sigma(\kappa_{\text{azimuthal}} + \kappa_{\text{axial}}) \tag{3.3}$$

where σ is surface tension, so the p can represent capillary pressure.

The 1D approximation of momentum equation of the flow can be expressed as

$$\rho(u_t + uu_z) = -p_z + 3\mu\frac{(h^2u_z)_z}{h^2} - \rho g \tag{3.4}$$

where ρ is density, u is velocity, p_z is pressure gradient with repect to z-axis, μ is viscosity and g is gravitational constant. Each variables can be scaled as

$$t = t^*\sqrt{\frac{\rho R^3}{\sigma}}, \quad z = z^*R, \quad h = h^*R, \quad u = u^*\frac{R}{t}, \quad p = p^*\frac{\sigma}{R}\mathrm{Oh} \tag{3.5}$$

Then dimensionless formulation of the (3.4) can be expressed as

$$u_t + uu_z = \left(-p_z + 3\frac{(h^2u_z)_z}{h^2}\right)\mathrm{Oh} - \mathrm{Bo} \tag{3.6}$$

In the demonstration complex fluids, the Ohnesorge number, ($Oh = \frac{\mu}{\sqrt{\rho\sigma R}}$) is $\gg 1$, meaning that the viscous force dominates over inertial and gravitational force, and Bond number, ($Bo = \frac{\rho g R^2}{\sigma}$) is $\ll 1$, meaning that surface tension dominates gravitatinal force. So the (3.6) can be simplified as,

$$p_z = 3\mu\frac{(h^2u_z)_z}{h^2} \tag{3.7}$$

The pressure gradient, p_z, determines the flow in the capillary-thinning thread, and the surface tension, σ, in the (3.3), is similar across all demonstration samples.

This implies that the curvatures of the thinning fluids and viscosity μ contain crucial information for predicting and estimating complex free surface flows.

Based on the above premise, we used a transformer model that specializes in deriving outputs while taking into account the context of the sequence. Using teacher forcing, we provided the model with time series curvatures as inputs and fluid mixing ratios as outputs. This approach allowed us to observe which sequences the model was paying attention to, and to more accurately identify regime transition points in complex fluids.

In this study, a blend of Carbopol, which has a distinct yield stress, and PEO, known for its viscoelastic properties, was selected as a demonstration sample.

3.2 Materials and Methods

Sample preparation

Table 3.1: Class-wise weight ratio of the multicomponent fluids. The total weight is set to 1 representing the weight ratios of each solution. The conctration of aqueous Carbopol (Lubrizol Korea, Inc.) solution is 0.14 %. The concentration of aqueous poly ethylene oxide ($M_v \sim 2.0 \times 10^6$ g/mol, Sigma Aldrich, Germany) solution is 1 %.

Solution	$r_{ey} = 0$	$r_{ey} = 0.25$	$r_{ey} = 0.50$	$r_{ey} = 0.75$	$r_{ey} = 1.00$
Carbopol	1.00	0.75	0.50	0.25	0
PEO	0	0.25	0.50	0.75	1.00

Curvature extraction

Before the curvature acquisition, captured images were processed using Canny edge detection. Two axisymmetric fluid edges were averaged and further post-processed through spline interpolation module in scipy of Python. The spline was interpolated with a degree of 5, defining the polynomial order of the spline, and 4 equally spaced knots, dividing the spline into segments. The curvature along the z-axis was obtained at 60 evenly spaced intervals, the curvature was calculated as the sum of $\kappa_{\text{axial}} + \kappa_{\text{azimuthal}}$.

In order to set the same initial internal pressure for the fluid regardless of the fluid type, the initial capturing time has been set from the point at which a specific curvature is formed at the minimum radius. This is the moment when the curvature of the minimum radius of the fluid is equal to the curvature corresponding to the nozzle radius. The curvature at the time t_{init} is defined as follows

$$\frac{1}{R_{\text{min,niddle}}} = \frac{1}{R_{\text{min,azimuthal}}} + \frac{1}{R_{\text{min,axial}}} \tag{3.8}$$

Finally, the end of the sequence is defined as the moment when capillary pressure of the minimum radius point reaches 5,000 Pa, which typically marks the onset of the beads-on-a-

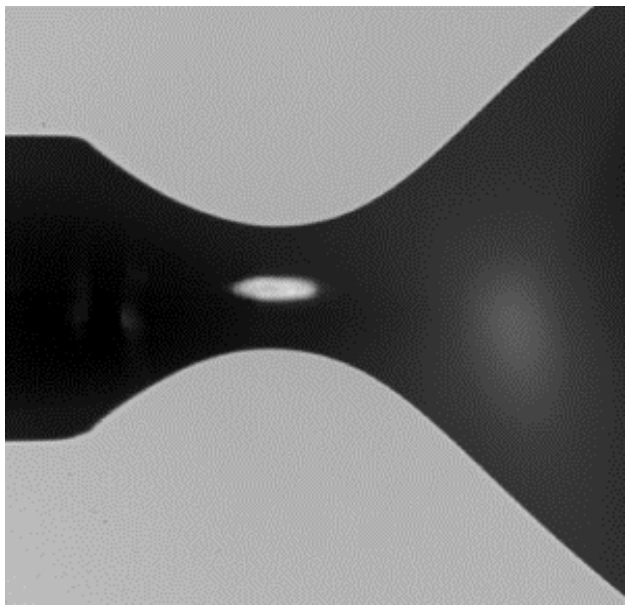

(a) Captured image

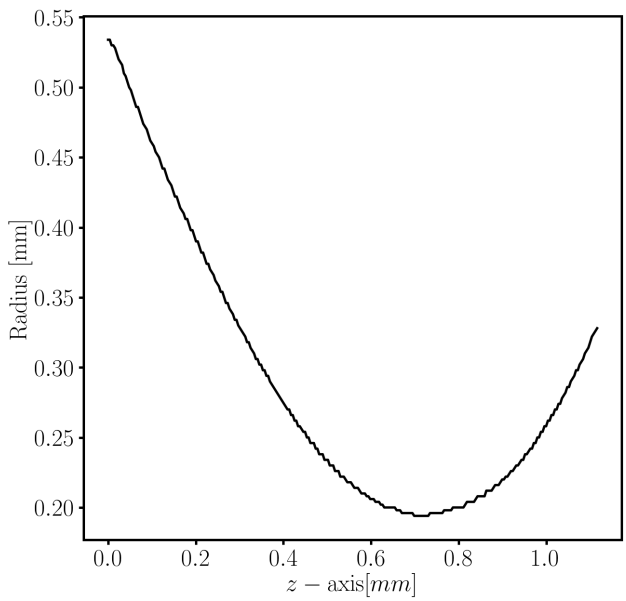

(b) Radius acquisition

Figure 3.1: Schematic process of radius acquisition.

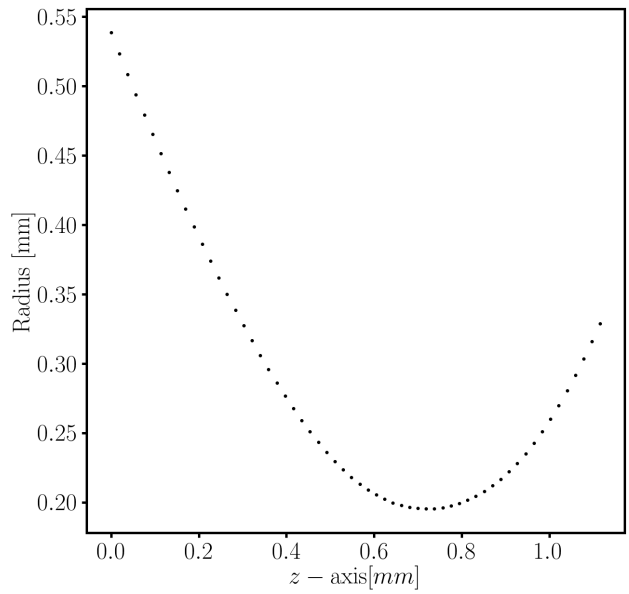

(a) Radius acquisition with 60-intervals

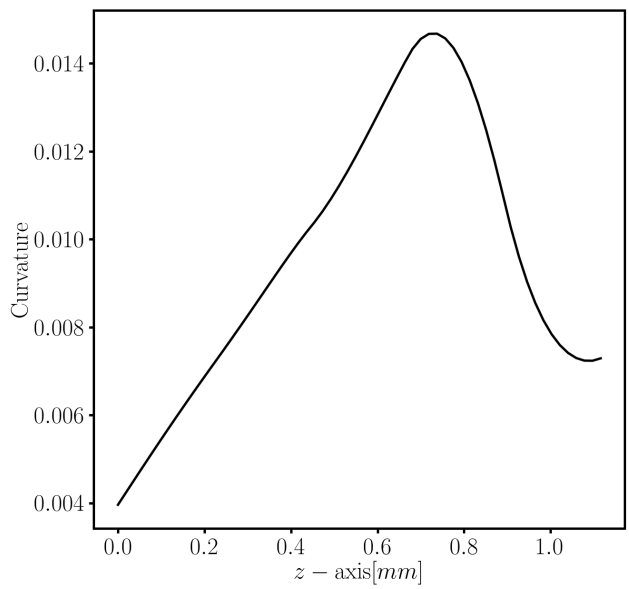

(b) Curvature acquisition with 60-intervals

Figure 3.2: Schematic process of curvature acquisition.

string phenomenon. In this region, the azimuthal curvature dominates over the axial curvature and could therefore signal the end of the sequence.

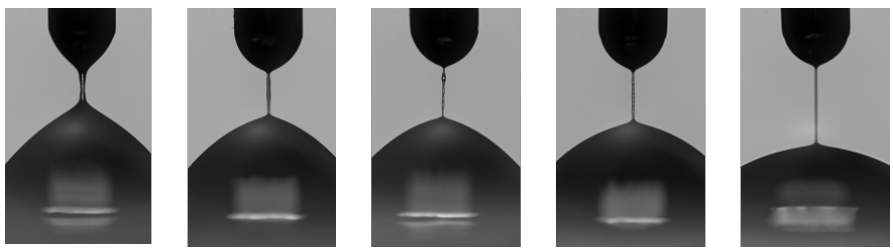

Figure 3.3: End of sequence

Model structure

In this study, only the encoder structure of the Transformer model was used. While the general structure of large language models (LLMs) is sequence-to-sequence, here we implemented a sequence-to-one structure to output a single value, specifically the ratio of PEO, from the time-series curvature. Additionally, layers and parameters were minimized to clarify the values extracted from the attention output.

In the multi-head attention mechanism, the model employs the concepts of query, key, and value to compute the attention output. The weights associated with the query, key, and value are multiplied with the embedded and the positional-encoded time-series curvature. Following this, the results are computed as

$$\text{Attention}(Q, K, V) = \text{softmax}(\frac{QK^T}{\sqrt{d_k}})V \tag{3.9}$$

where Q, K and V represents the query, key and value, respectively, while d_k denotes model dimension, which serves as scaling factor. In this context, the operations involving the Q and K are utilized in the self-attention mechanism, which signifies the relationships among sequences. Meanwhile, V represents the crucial sequences for deriving the output. By combining these three parameters, the contextual information and significance of the sequences can be effectively represented in the attention output. After that, attention output add to input and layer normalized as

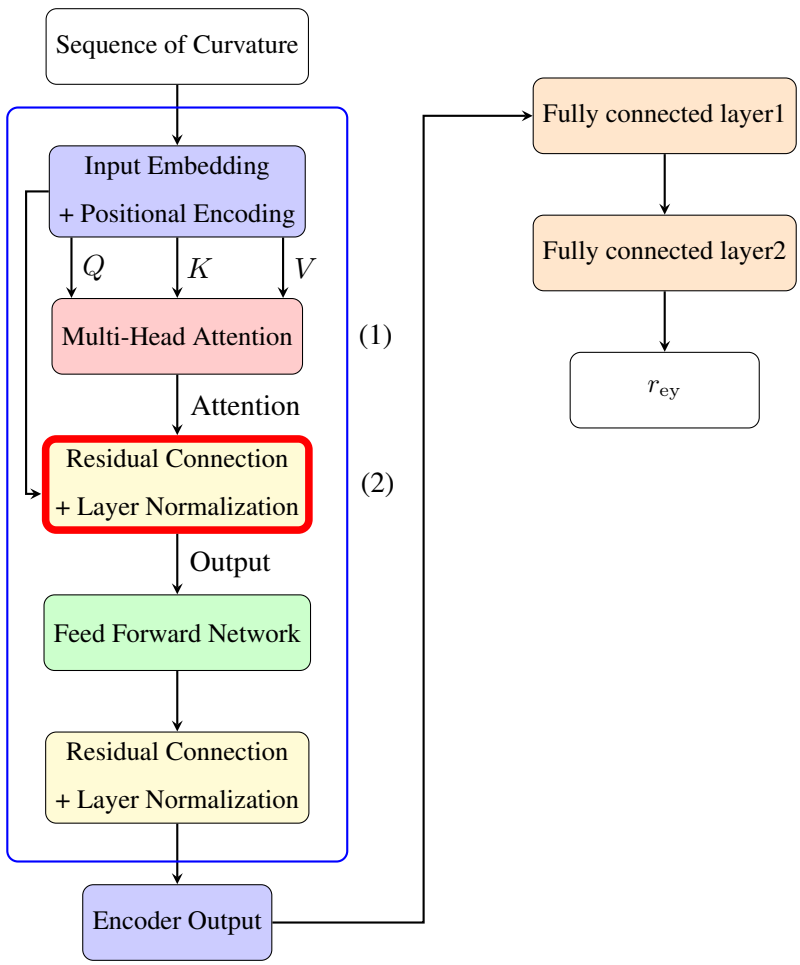

Figure 3.4: Transformer Encoder Structure

$$\text{Output} = \text{LayerNorm}(x + \text{Attention}) \tag{3.10}$$

where x is input vecter before pass through the (1), and LayerNorm is defined as

$$\text{LayerNorm}(x) = \frac{x - \mu}{\sqrt{\sigma^2 + \epsilon}} \cdot \gamma + \beta \tag{3.11}$$

where μ is the mean and σ is the variance of the vector x with respect to $d_{\text{model}} = 64$ in this study. ϵ is a small constant for numerical stability, and γ and β are learnable parameters that adjust the scale and shift of the normalized outputs. The dimensions and parameters of the model are described in the table.

Table 3.2: Dimensions of the model.

d_{input}	$d_{\text{embedding}}$	d_{query}	d_{key}	d_{value}	d_{fcl}	d_{out}
seq $\times$ 60	seq $\times$ d_{model}	seq $\times$ d_{model}	seq $\times$ d_{model}	seq $\times$ d_{model}	$1 \times (\text{seq} \cdot 60)$	1

Table 3.3: Parameters of the model.

Loss Function	Epoch	Learning rate	Data	Optimizer
MSE	10^3	10^{-5}	10 pcs each	Adam

All input sequences were padded to match the maximum sequence length. In this study, we focused on the Output value, which allowed us to more clearly identify the differences present among the samples through the aforementioned process.

3.3 Results and Discussion

Attention Output

The output values for the sequence are L1 norm normalized by class in the direction of the d_{model}. It can be seen that as the ratio of PEO increases, the time t_{c} at which the maximum output appears, arrives quickly, and we define the interval between t_0 and t_{c} as λ_{eff}.

$$\lambda_{\text{eff}} = t_0 - t_{\text{c}} \tag{3.12}$$

We assumed this λ_{eff} to be the region where relaxation occurs as the fluid undergoes extension, and we found that it increases linearly with the proportion of PEO.

Physical meaning of t_c

To investigate the physical significance of t_c, a qualitative analysis was first conducted using recorded video footage. The results revealed that, prior to t_c, the fluid exhibited a concave and asymmetrical shape, centered around the minimum radius. After t_c, the fluid transitioned to a locally cylindrical and symmetrical shape, as shown in Fig. 3.6.

In order to quantify the observed qualitative features, the temporal changes in p were measured at the minimum radius and at two points symmetrical to the minimum radius. The locations for evaluating p at t_{c} are shown in Fig. 3.8, and the graphs illustrating the maximum p values at each location over time are presented in Fig. 3.9. As shown in Fig. 3.9, it was observed that at t_c, p exhibits symmetry around the minimum radius. From this point onward, the thread transitions into a cylindrical structure, and the stress was found to develop exponentially after this point. Furthermore, the observation that the fluid shape becomes symmetrical after the t_c suggests that the gravitational influence on the fluid remaining in the thread is minimized as the fluid initially within the thread drains toward the substrate. Beyond this point, the flow of the fluid within the thread is governed by the competition between the capillary pressure and the inherent rheological properties of the fluid resisting it. The analysis of the exponentially increasing capillary pressure p after t_c means that it focuses on the dynamic interplay between the capillary pressure driving the flow within the cylindrical fluid structure and the inherent viscoelasticity of the fluid opposing it. In other words, the analysis of the exponentially increasing capillary pressure p after t_c means that it focuses on the dynamic interplay between the capillary pressure driving the flow within the cylindrical fluid structure and the inherent viscoelasticity of the fluid opposing it. As shown in Fig. 3.7, it is assumed that a significant change occurs at the t_c time point depending on the fluid composition. By applying the pixel intensity emphasis point discussed in Chapter 2, it was found that the method yields higher accuracy.

The following section decomposes the stress components and derives the rheological properties accordingly.

Explicit model of Henky strain

In this section, the stress, σ, is decomposed using the Kelvin-Voigt model (Bulıcek *et al.* (2012)), and the parameter k, associated with the resistance to stress growth, named as $stressresistancetime$ in this research, is determined. The viscosity, η, and relaxation time, λ, are then calculated, and the Hencky strain after t_c is derived based on these parameters. The internal thread stress, σ, after t_c, is experimentally observed to increase exponentially. This behavior can be expressed with an ansatz as follows,

$$\sigma = \sigma_0 e^{t/k} \tag{3.13}$$

Where σ_0 is the stress at t_c and k is the stress resistance parameter, and σ can be decomposed as follows based on the Kelvin-Voigt model.

$$\frac{\sigma_0}{\eta} e^{t/k} = \frac{\epsilon}{\lambda} + \dot{\epsilon} \tag{3.14}$$

Where η, ϵ, λ, and $\dot{\epsilon}$ are viscosity, Henky strain, relaxation time, and Henky strain rate, respectively. When integrating the equation with respect to time,

$$\epsilon = \frac{\sigma_0}{\eta} \frac{e^{t/k}}{\frac{1}{k} + \frac{1}{\lambda}} \tag{3.15}$$

As shown in (3.3), an explicit expression for Henky strain can be obtained. The proposed rheological properties determining the Hencky strain were obtained first by fitting k through (3.3) and the measured p at the minimum radius, and subsequently by fitting through (3.3) and the measured ϵ. As shown in Fig. 3.10, it was observed that the exponential development of stress after t_c matches well, except for the pure Carbopol fluid. This trend is presumed to result from the influence of PEO, which relaxes the stress generated during the extension of the fluid. As mentioned in the previous section, this is thought to begin when p becomes symmetrical around the minimum radius. The value of k corresponds to λ_E, which depends

on the concentration of PEO, as derived in the study by the Sharma group (Dinic & Sharma (2019)).

The value of k obtained through the above process is substituted into (3.3), and η and λ are determined through fitting with the measured ϵ. The results are plotted in Fig. 3.11

Table 3.4: Rheological parameters derived from experimental data and model fitting.

Solution	$r_{ey} = 0$	$r_{ey} = 0.25$	$r_{ey} = 0.50$	$r_{ey} = 0.75$	$r_{ey} = 1.00$
k	0.0124	0.0137	0.0187	0.0159	0.0345
η	3.1764	3.8068	7.6906	2.0628	7.7533
λ	17×10^4	0.0076	0.0150	0.0033	0.0081

The final rheological properties obtained for each fluid are summarized in Tab. 3.3 The stress resistance time k has a more significant impact on the p and Hencky strain after t_c than the λ derived from the Kelvin-Voigt model. The value of k can serve as a measure of how much the formation of curvature within the thread is delayed, which is related to the delay in BOAS formation caused by perturbations in complex fluids. On the other hand, η, being an anisotropic tensor according to the rate of deformation tensor, was fitted as a fixed scalar value under the assumption that the change of η after t_c is negligible. For further improvement in parameter derivation, a model suitable for numerical analysis, such as the Giesekus model, could be used to achieve more accurate parameter estimation (Gauri & Koelling (1997)).

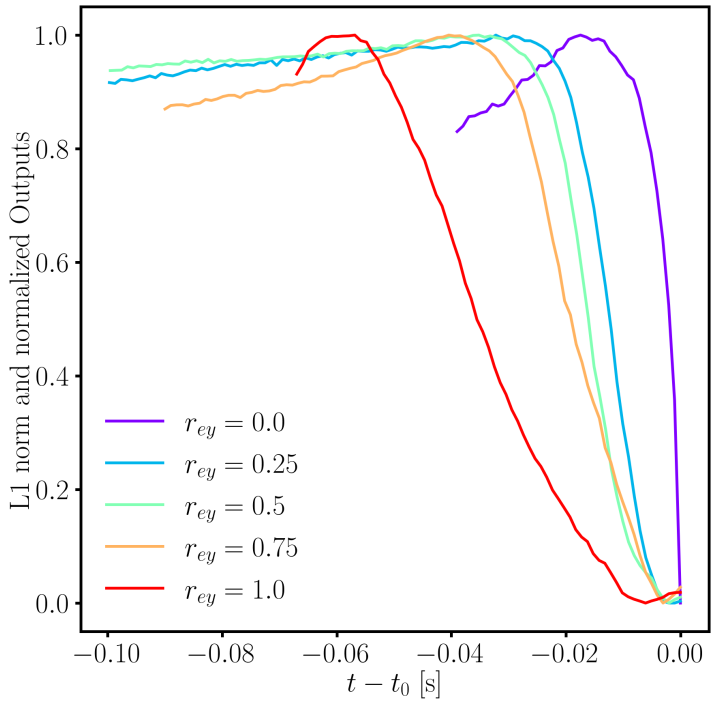

(a) Time evolution of output value.

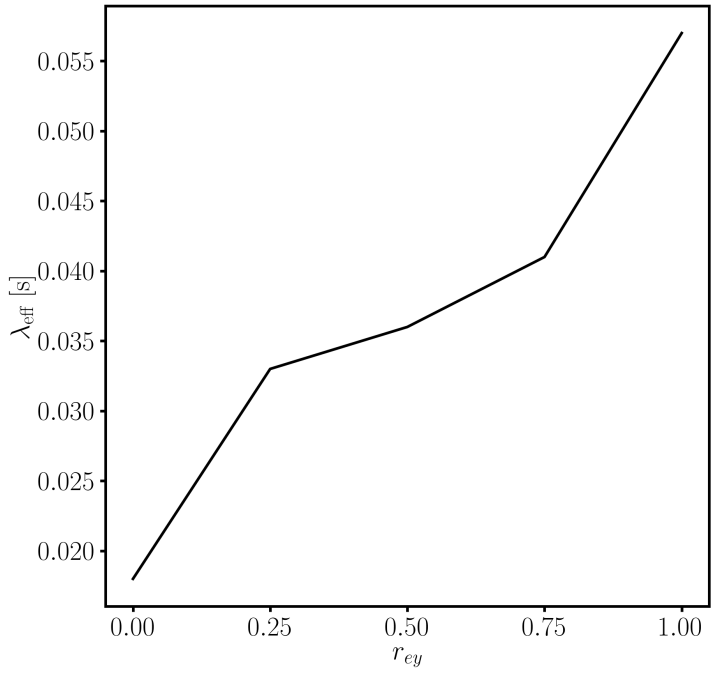

(b) Effective relaxation time according to r_{ey}.

(a) $r_{ey} = 0.0$

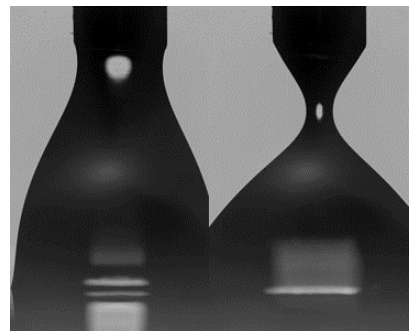

(b) $r_{ey} = 0.25$

(c) $r_{ey} = 0.5$

(d) $r_{ey} = 0.75$

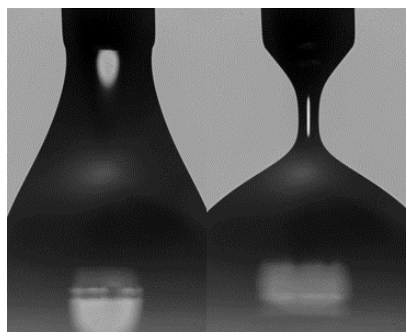

(e) $r_{ey} = 1.0$

Figure 3.6: Comparative images of the shape at t_{init} and t_c for each sample show that, compared to t_{init} , the fluid transitions to a symmetric and locally cylindrical shape around the minimum diameter at t_c.

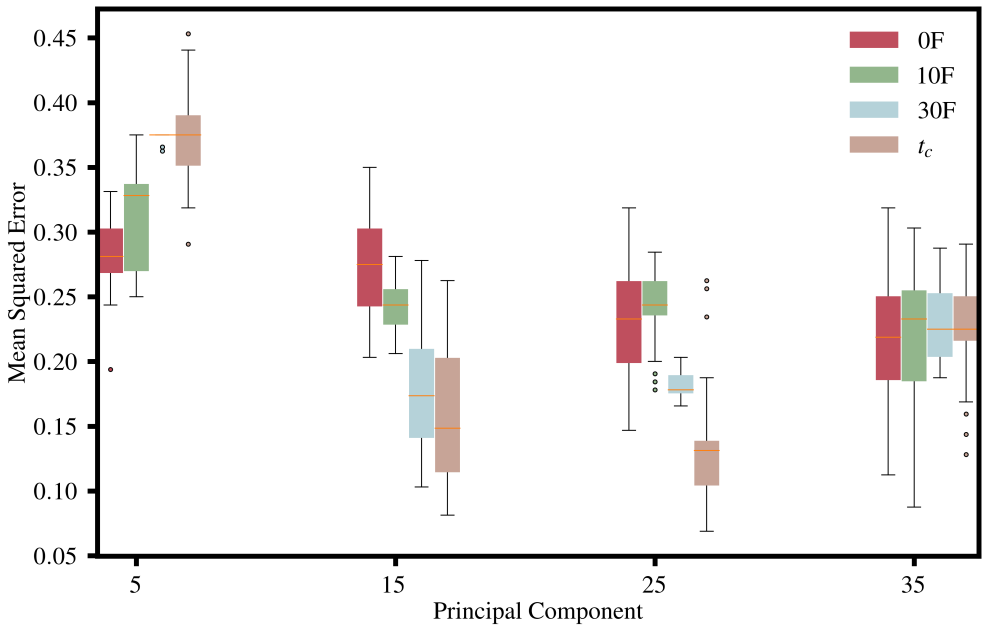

Figure 3.7: The boxplot showing the accuracy of composition ratio prediction using cumulative images. By emphasizing the images after the t_c time point, it was found that a lower MSE (Mean Squared Error) was achieved.

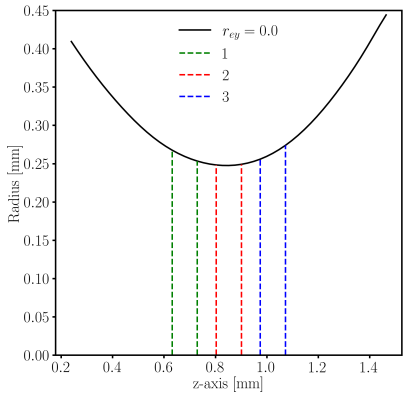

(a) $r_{ey} = 0.0$

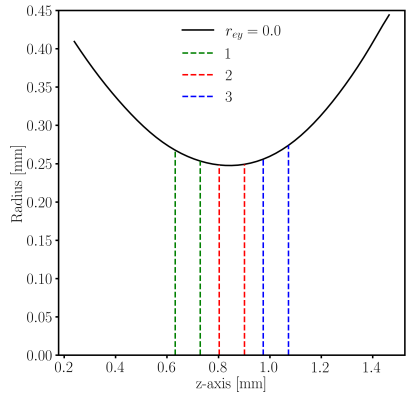

(b) $r_{ey} = 0.25$

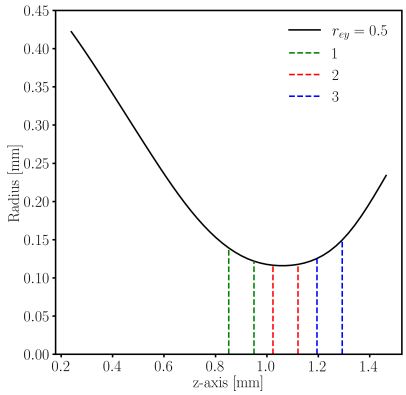

(c) $r_{ey} = 0.5$

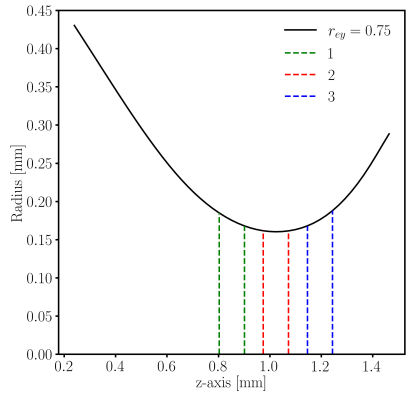

(d) $r_{ey} = 0.75$

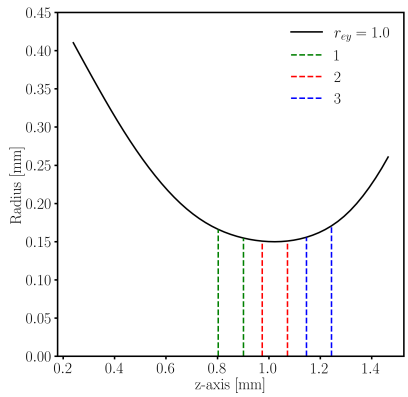

(e) $r_{ey} = 1.0$

Figure 3.8: The p values along the z-axis at t_c and the range of p for symmetry verification are shown. The direction of gravity is to the right, with 1 indicating the nozzle and 3 indicating the substrate.

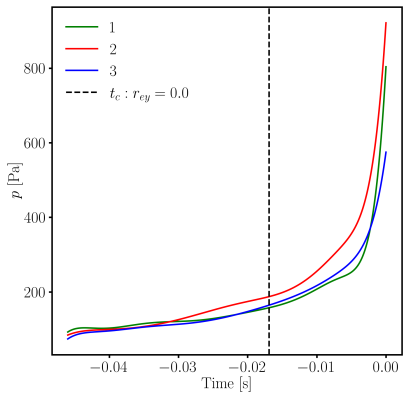

(a) $r_{ey} = 0.0$

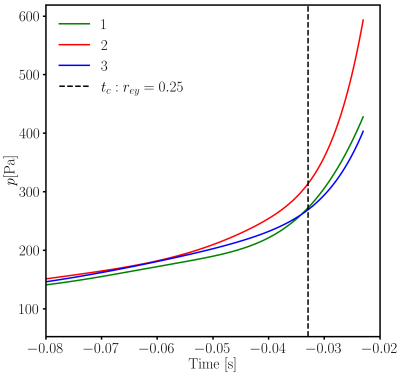

(b) $r_{ey} = 0.25$

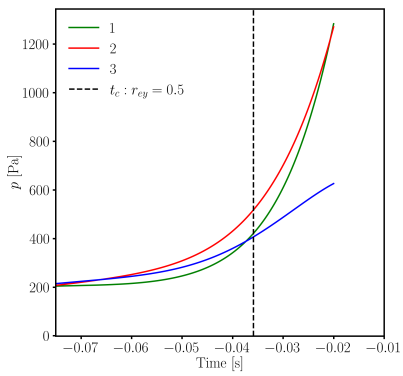

(c) $r_{ey} = 0.5$

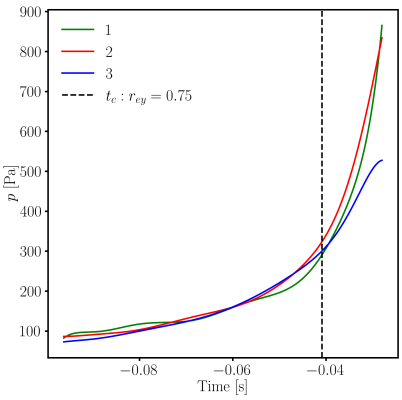

(d) $r_{ey} = 0.75$

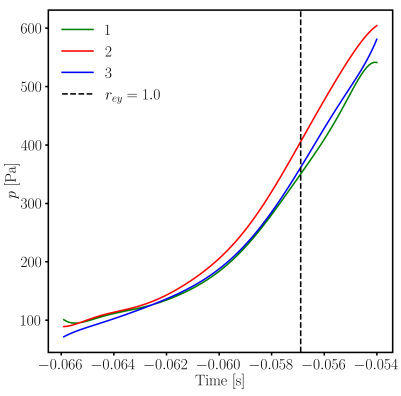

(e) $r_{ey} = 1.0$

Figure 3.9: The p graphs for each thread position over time for each sample are shown, with the positions corresponding to those indicated in Fig. 3.8

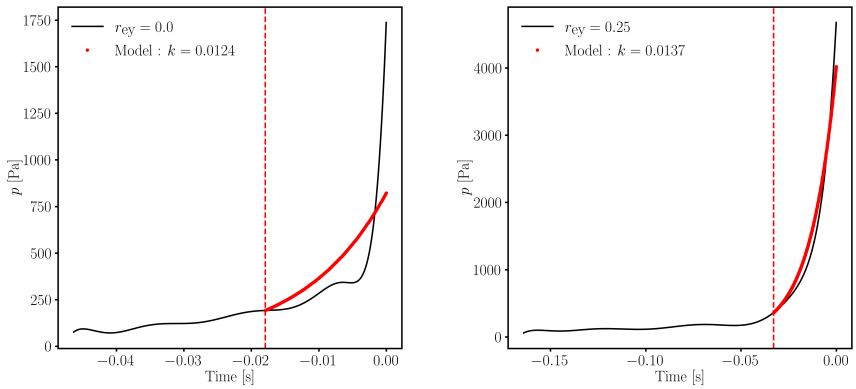

(a) $r_{ey} = 0.0$

(b) $r_{ey} = 0.25$

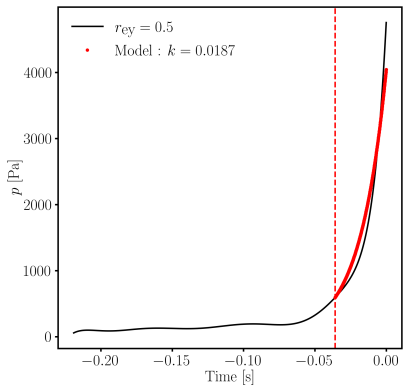

(c) $r_{ey} = 0.5$

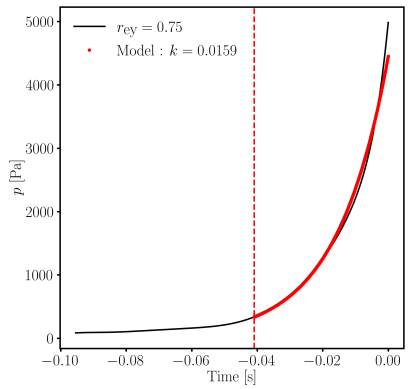

(d) $r_{ey} = 0.75$

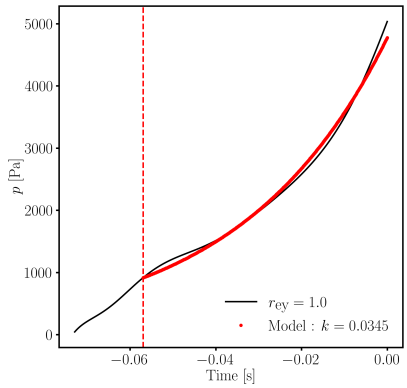

(e) $r_{ey} = 1.0$

Figure 3.10: The fitting results between the capillary pressure measured through curvature and (3.3).

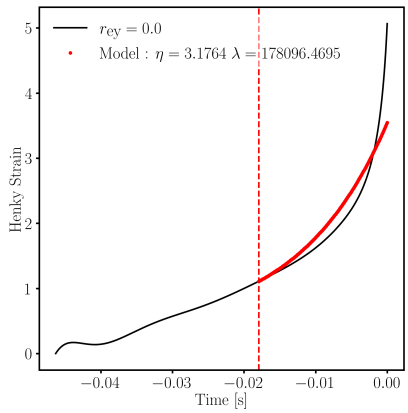

(a) $r_{ey} = 0.0$

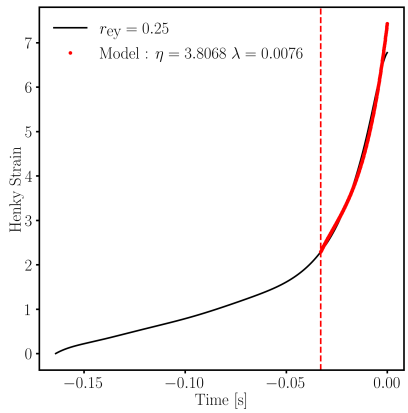

(b) $r_{ey} = 0.25$

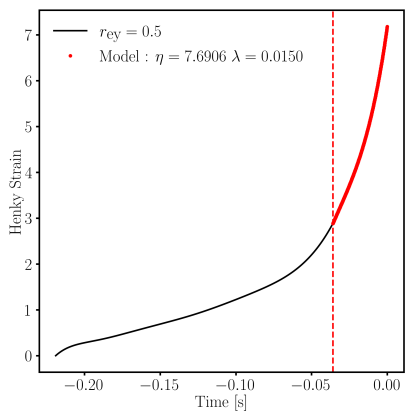

(c) $r_{ey} = 0.5$

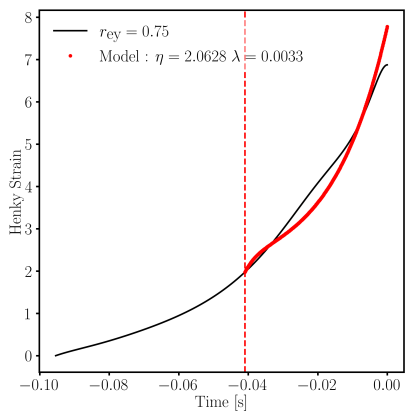

(d) $r_{ey} = 0.75$

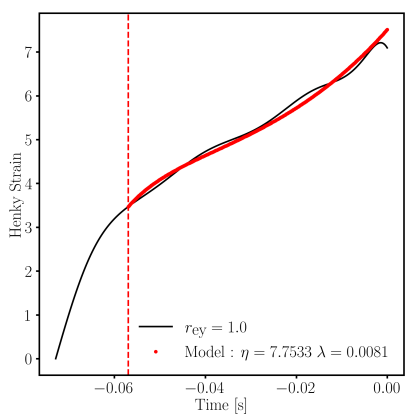

(e) $r_{ey} = 1.0$

Figure 3.11: The fitting results between the Henky strain measured through radius and (3.3).

Chapter 4

Final remarks

This thesis investigates the capillary thinning dynamics of complex fluids using innovative visualization techniques and machine learning. Chapter 2 presents an analysis based on cumulative images and statistical approaches, which reveal the relative rheological properties of fluids within a dataset. This approach allows for the classification of fluids and estimation of their approximate composition without relying on traditional rheological models. However, composition estimation required user expertise, cumulative images lacked sequential information, and PCA methods based on pixel variation were limited in handling position invariance.

To address these limitations, Chapter 3 describes a study where fluid curvature was extracted from edge shapes across the sequence and analyzed using the transformer model, which excels at capturing contextual information within sequences. This method enabled the identification of critical turning points, facilitating focused analysis at these points and offering the opportunity for a more comprehensive investigation of the pressure distribution within the filament, especially in previously difficult-to-analyze singularity regions.

This work aims to contribute to the quantitative differentiation and analysis of fluid properties in extensional flow at free interfaces, thereby advancing our understanding of free surface extensional flow.

Bibliography

ABDI, HERV & WILLIAMS, LYNNE J 2010 Principal component analysis. *Wiley interdisciplinary reviews: computational statistics* **2** (4), 433–459.

ADE, SOMESHWAR SANJAY, CHANDRALA, LAKSHMANA DORA & SAHU, KIRTI CHANDRA 2023 Size distribution of a drop undergoing breakup at moderate weber numbers. *Journal of Fluid Mechanics* **959**, A38.

ADE, SOMESHWAR SANJAY, GUPTA, DEEPA, CHANDRALA, LAKSHMANA DORA & SAHU, KIRTI CHANDRA 2024 Application of deep learning and inline holography to estimate the droplet size distribution. *International Journal of Multiphase Flow* **177**, 104853.

BHAT, PRADEEP P, APPATHURAI, SANTOSH, HARRIS, MICHAEL T, PASQUALI, MATTEO, MCKINLEY, GARETH H & BASARAN, OSMAN A 2010 Formation of beads-on-a-string structures during break-up of viscoelastic filaments. *Nature Physics* **6** (8), 625–631.

BULICEK, M, MÁLEK, J & RAJAGOPAL, KR 2012 On kelvin–voigt model and its generalizations. *Evol. Equ. Control Theory* **1** (1), 17–42.

CANNY, JOHN 1986 A computational approach to edge detection. *IEEE Transactions on Pattern Analysis and Machine Intelligence* **8** (6), 679–698.

CHANG, HSUEH-CHIA, DEMEKHIN, EVGENY A & KALAIDIN, EVGENY 1999 Iterated stretching of viscoelastic jets. *Physics of fluids* **11** (7), 1717–1737.

DINIC, JELENA, JIMENEZ, LEIDY NALLELY & SHARMA, VIVEK 2017 Pinch-off dynamics and dripping-onto-substrate (dos) rheometry of complex fluids. *Lab Chip* **17**, 460–473.

DINIC, JELENA & SHARMA, VIVEK 2019 Macromolecular relaxation, strain, and extensibility determine elastocapillary thinning and extensional viscosity of polymer solutions. *Proceedings of the National Academy of Sciences* **116** (18), 8766–8774.

DINIC, JELENA & SHARMA, VIVEK 2020 Power laws dominate shear and extensional rheology response and capillarity-driven pinching dynamics of entangled hydroxyethyl cellulose (hec) solutions. *Macromolecules* **53** (9), 3424–3437.

DINIC, JELENA, ZHANG, YIRAN, JIMENEZ, LEIDY NALLELY & SHARMA, VIVEK 2015 Extensional relaxation times of dilute, aqueous polymer solutions. *ACS Macro Letters* **4** (7), 804–808.

DINO, HIVI ISMAT & ABDULRAZZAQ, MAIWAN BAHJAT 2019 Facial expression classification based on svm, knn and mlp classifiers. In *2019 International Conference on Advanced Science and Engineering (ICOASE)*, pp. 70–75.

EGGERS, J., HERRADA, M. A. & SNOEIJER, J. H. 2020 Self-similar breakup of polymeric threads as described by the oldroyd-b model. *Journal of Fluid Mechanics* **887**, A19.

ENTOV, VM & HINCH, EJ 1997 Effect of a spectrum of relaxation times on the capillary thinning of a filament of elastic liquid. *Journal of Non-Newtonian Fluid Mechanics* **72** (1), 31–53.

GAO, JIAN, GUILDENBECHER, DANIEL R, REU, PHILLIP L, KULKARNI, VARUN, SOJKA, PAUL E & CHEN, JUN 2013 Quantitative, three-dimensional diagnostics of multiphase drop fragmentation via digital in-line holography. *Optics letters* **38** (11), 1893–1895.

GAURI, VISHAL & KOELLING, KURT W 1997 Extensional rheology of concentrated poly (ethylene oxide) solutions. *Rheologica Acta* **36**, 555–567.

GUILDENBECHER, DANIEL R, GAO, JIAN, CHEN, JUN & SOJKA, PAUL E 2017 Characterization of drop aerodynamic fragmentation in the bag and sheet-thinning regimes by crossed-beam, two-view, digital in-line holography. *International journal of multiphase flow* **94**, 107–122.

GUO, MENG-HAO, LU, CHENG-ZE, LIU, ZHENG-NING, CHENG, MING-MING & HU, SHI-MIN 2022 Visual attention network. https://arxiv.org/pdf/2202.09741, accessed on 2024-07-22.

JAMES, GARETH, WITTEN, DANIELA, HASTIE, TREVOR, TIBSHIRANI, ROBERT & JONATHAN 2013 *An introduction to statistical learning*, , vol. 112. Springer.

KOLAROVA RASKOVA, ZUZANA, HRABALIKOVA, MARTINA & SEDLARIK, VLADIMIR 2016 Effect of sodium salicylate on the viscoelastic properties and stability of polyacrylate-based hydrogels for medical applications. *International Journal of Polymer Science* **2016** (1), 5614687.

MCKINLEY, GARETH H 2005 Visco-elasto-capillary thinning and break-up of complex fluids. *Journal of Non-Newtonian Fluid Mechanics* pp. 10–23.

MCKINLEY, GARETH H & SRIDHAR, TAMARAPU 2002 Filament-stretching rheometry of complex fluids. *Annual Review of Fluid Mechanics* **34** (1), 375–415.

MEDSKER, LARRY R & JAIN, LC 2001 Recurrent neural networks. *Design and Applications* **5** (64-67), 2.

MUDDU, RAJESWARI J., LU, JIAKAI, SOJKA, PAUL E. & CORVALAN, CARLOS M. 2012 Threshold wavelength on filaments of complex fluids. *Chemical Engineering Science* **69** (1), 602–606.

NIEDZWIEDZ, K, ARNOLDS, O, WILLENBACHER, N & BRUMMER, R 2009 How to characterize yield stress fluids with capillary breakup extensional rheometry (caber)? *Applied Rheology* **19** (4), 41969.

OPENCV DEVELOPMENT TEAM 2021 Open Source Computer Vision Library, Version 4.7.0. https://opencv.org/releases/, accessed on 2023-06-01.

O'SHEA, KEIRON AND NASH, RYAN 2015 An Introduction to Convolutional Neural Networks. https://arxiv.org/pdf/1511.08458, accessed on 2024-07-22.

PEDREGOSA, FABIAN, VAROQUAUX, GAËL, GRAMFORT, ALEXANDRE, MICHEL, VINCENT, THIRION, BERTRAND, GRISEL, OLIVIER, BLONDEL, MATHIEU, PRETTENHOFER, PETER, WEISS, RON & DUBOURG, VINCENT 2011 Scikit-learn: Machine learning in python. *the Journal of machine Learning research* **12**, 2825–2830.

RODD, LUCY E., SCOTT, TIMOTHY P., COOPER-WHITE, JUSTIN J. & MCKINLEY, GARETH H. 2005 Capillary break-up rheometry of low-viscosity elastic fluids. *Applied Rheology* **15** (1), 12–27.

SINGH, ABHISHEK & KUMAR, SAURABH 2012 Face recognition using pca and eigen face approach. PhD thesis, National Institute of Technology.

ZHANG, DIANA Y & CALABRESE, MICHELLE A 2022 Temperature-controlled dripping-onto-substrate (dos) extensional rheometry of polymer micelle solutions. *Soft Matter* **18** (20), 3993–4008.

ZHANG, JUN, YAN, YONG & LADES, MARTIN 1997 Face recognition: eigenface, elastic matching, and neural nets. *Proceedings of the IEEE* **85** (9), 1423–1435.

국문 초록

미세유체의 자유계면 신장 유동 역학은 잉크젯 인쇄, 에멀젼 형성 등 다양한 응용 분야에서 중요한 연구 주제이다. 그러나 기존의 Slender-Jet 근사는 단일 지점에서의 측정에 집중하여 복잡한 유체 형상의 시공간적 진화를 부분적으로만 포착하는 한계가 있다. 이러한 형상은 유변학적 특성을 포함하고 있음에도, 기존의 분석 방법으로는 해당 정보를 온전히 추출하기 어렵다.

본 연구에서는 유변학적 모델에 의존하지 않고 유체 흐름을 정량적으로 특성화하기 위해 머신 러닝과 유동 시각화를 결합한 새로운 접근법을 제안한다. 제안된 방법은 자유계면 신장 흐름의 시공간적 특성을 관찰하기에 최적화된 DoS-CaBER (Dripping onto Substrate Capillary-Breakup Extensional Rheometry) 기법으로 캡처한 이미지를 활용한다. 이 기법을 통해 누적 이미지와 가장자리 곡률을 분석함으로써 유동에 대한 포괄적인 정보를 추출할 수 있으며, 자유 표면 신장 유동의 특이 동역학을 보다 정밀하게 분석할 수 있다. 본 접근법은 비뉴턴 유체의 복잡한 유동 역학을 이해하는 데 중요한 분석 도구가 될 것으로 기대된다.

주요어: 신장 유동, 흐름 시각화, 알고리즘, 기계 학습

학번: 2021-36497

감사의 글

I would like to express my sincere gratitude to Professor Jae-Wook Nam for his unwavering support and invaluable guidance throughout my Ph.D. research. His mentorship has been instrumental in the successful completion of this study.

My sincere thanks also go to Professor Ju Min Kim for his assistance in benchmarking and internalizing the DoS-CaBER system, which contributed significantly to the depth of this research.

I am deeply grateful to Jun-Hyeong Jang for his collaborative efforts in developing the measurement system, visualisation code, and implementation of machine learning techniques, all of which were crucial to the progress of my work.

I would also like to thank Dong Keun Yu, who provided insightful guidance and helped me overcome various challenges with his experience and wisdom.

Finally, I would like to express my deep gratitude to my wife, whose unwavering support and understanding allowed me to dedicate myself to my research while raising our two children.

Chapter 5

Supplementary Information